Surface Rupture Detection with Support Vector Machine Classification:

Case Study from Ridgecrest, CA

by

Jordan M. Cooper

A Thesis Presented to the
FACULTY OF THE USC DORNSIFE COLLEGE OF LETTERS, ARTS AND SCIENCES
University of Southern California
In Partial Fulfillment of the
Requirements for the Degree
MASTER OF SCIENCE
(GEOGRAPHIC INFORMATION SCIENCE AND TECHNOLOGY)

August 2021

To my beautiful wife and daughter

Acknowledgements

Thank you to my advisor Dr. Fleming for his support, advice, and understanding throughout this thesis. Also, thank you to my committee members for their recommendations, which helped make this thesis project better. Additional thank you to Dr. Vos and the staff at the USC SSI for their assistance and support during a trying time. The USGS and the various teams that collected the data used in this thesis should also be thanked.

Table of Contents

List of Tables

List of Figures

Abbreviations

GIS	Geographic information system
GISci	Geographic information science
SSI	Spatial Sciences Institute
TIFF	Tagged Image File Format
UAV	Unmanned Aerial Vehicle
UAS	Unmanned Autonomous System
USGS	United States Geological Survey
USC	University of Southern California

Abstract

One possible costly outcome of large earthquakes is breakages in the ground surface, known as surface ruptures. Surface ruptures can cause damage to human infrastructure as well as harm humans. Detailed field studies that trace these structures take substantial time and effort because they affect large regions, but this is reducible by collecting remote sensed imagery performing supervised classification on the imagery with a GIS. For this study, unmanned aerial vehicles (UAV) imagery from the Ridgecrest area in California was analyzed using the support vector machine (SVM) classification method to attempt surface rupture detection in desert terrain. The imagery covers a small area, so a K-Folds analysis method was used to attain statistically significant results. This involved splitting the imagery into 5 random pools of 30-meter by 30-meter squares before running the classification. The results of each classification were analyzed by generating confusion matrices and visual inspection. An average of the five confusion matrices was used for a final analysis. While this method did classify larger segments (> 0.5-meter-wide) of surface rupture that was in the image, it missed most of the smaller surface rupture segments (< 0.5-meter-wide). In addition, the technique misclassified parts of the imagery as surface rupture, especially around the vegetation, road paths, and amongst a rock field in the south-east corner. Further testing should be done with this method, including using it on imagery with different land-cover. Based on the results of the further testing it may be ready to try in practice scenarios for real-life earthquake disasters.

Chapter 1 Introduction

One of the natural disasters that cause the most significant damage to human-made structures and loss of life is earthquakes. From 2009 to 2019, 27,193 deaths were attributable to earthquakes, 47.7% of the 56,967 recorded natural disaster deaths occurred worldwide during that period (CRED 2020). During that same period earthquake also caused 44.6 billion U.S. dollars in economic losses. While earthquakes can cause damage in various ways, the most damaging source is surface ruptures (Jin and Kim 2020). Surface ruptures are cracks in the ground that can be anywhere from a few meters in length to several kilometers and can have vertical offset up to six meters. The ruptures are associated with large earthquakes greater than 6.0 Mw. The San Fernando Earthquake in 1971 led to the Alquist-Priolo Earthquake Fault Zoning Act in California, which prevents building occupied structures on active faults that can cause surface ruptures. Surface ruptures were observable following earthquakes worldwide, such as in the 1999 Chi-Chi, Taiwan earthquake, and the 2003 Bam, Iran earthquake. These earthquakes caused damage to many buildings and had high fatality rates, with 2000 people who died in Chi-Chi and at least 25000 died in Bam. Much of the destruction was associated with surface ruptures.

In this thesis, remote sensed imagery was classified, mapping the potential location of surface ruptures in imagery from a study site near Ridgecrest, California. This site experienced an earthquake sequence that involved over 100,000 total earthquakes larger than 0.5 Mw. Amongst all of these the earthquakes that were the most powerful were a 6.4 Mw on July 4th, 2019 and a 7.1 Mw on July 5th, 2019. While different satellite and aerial systems for collecting remote sensed imagery exist, this thesis only used imagery from high spatial resolution cameras mounted on unmanned aerial vehicles (UAV). The raster imagery used came from a collection of

imagery captured at two approximately 500-meter by 500-meter sites over six days between July 7th, 2019 and September 27th, 2019. The imagery, captured on July 11th, of a segment of the surface rupture produced by the 7.1 Mw earthquake was used because of the data's good quality. This thesis aims to classify the imagery to differentiate between surface ruptures and the surrounding area. With a real-world application in mind for this project, the methods used were selected for ease of use. Also, the methods should be able to analyze raster imagery and find surface ruptures following large earthquakes to aid rescue crews and repair teams, as well as policymakers.

1.1. Surface Rupture Mapping

Surface ruptures are cracks in the ground that are usually formed from earthquakes 6.0 Mw or greater in strength (see Figure 1). The ruptures are either primary ruptures, where the earthquake fault extends to the surface, or secondary, where the earthquake fractures the surface outside the earthquake fault plane. The creation of the ruptures can cause damage to utilities, transportation infrastructure, and buildings with people in them. Rapid mapping of these ruptures, along with infrastructure plans, would allow for quick response to earthquakes like the 2019 Ridgecrest Earthquake sequence.

Figure 1 Surface Rupture located near the maximum displacement from the Mw 7.1 earthquake (Image Source: Jet Propulsion Laboratory, October 17, 2019).

The 2019 Ridgecrest Earthquake sequence generated two sets of surface ruptures when the two largest earthquakes occurred, a 7.1 Mw mainshock and a 6.4 Mw foreshock. When investigating the earthquakes, researchers used various methods, including satellite imagery, aerial imagery, and field investigations. From their studies, the researchers established the different characteristics of the ruptures generated from the two earthquakes. The 7.1 Mw displacement was right lateral with up to 7.0 m of movement though displacement was mainly in the range of 1.2-1.7 m. 66% of the displacement occurred around the earthquake's epicenter over a 12 km section of the surface rupture. The 6.4 Mw was left lateral with up to 1.6 m of movement on an individual strand, though most movement was in the range of 0.3-0.5 m.

1.2. Classification of Remotely Sensed UAV Imagery

Methods used during this thesis were based on a methodology previously used to classify ground cracks in a coal mining area using UAV imagery (Zhang et. al. 2020). Traditionally classification is performed by a researcher going through each image and marking the location of the object of interest; in this case, it is surface ruptures. This can be a time-intensive endeavor. With the advent of faster and more powerful computers, that task is simplified with automatic classification methods, both supervised and unsupervised. During this project a supervised method, SVM classification, was used in ArcGIS Pro. The software used training data to teach the software the optical properties of the surface ruptures to classify it from the imagery that was provided. An explanation of A further explanation on the classification methods is found in Chapter 3.

In a GIS, Support Vector Machine algorithm is a supervised machine learning methodology that is used to classify raster imagery. Classes are defined based on hyperplanes that define the boundaries of the classes. A hyperplane in geometry is a subspace that has one

less dimension than the surrounding space, splitting the surrounding dimension into two parts (See Figure 2). In machine learning, hyperplanes are the boundaries that separate different classes. The hyperplane is plotted to fit between the groups of data points for the different classes defined in the training data. Hyperplanes can usually fit several different orientations, but the one that is selected fits between the closest data points on both sides in such a way that they will have the greatest possible distance or margin from those data points (See Figure 2).

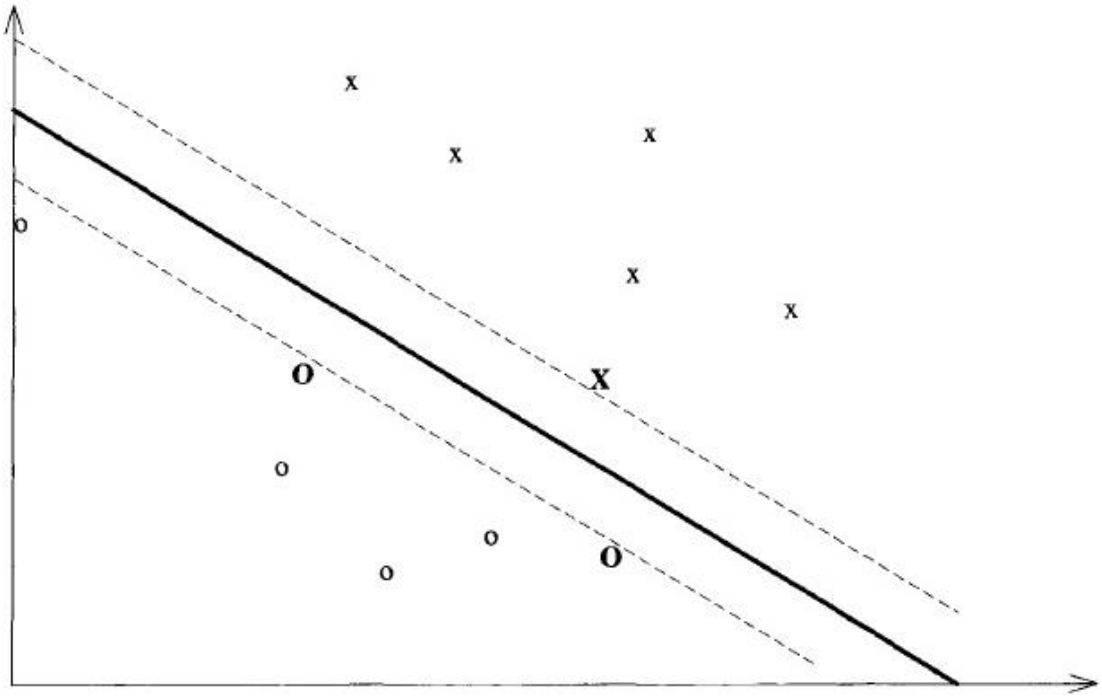

Figure 2 Datasets x and o separated by a hyperplane. Dashed lines represent the maximum margins. Bold X and O's are data points used to find the margins.

1.3. Study Area

The study area is a part of the Eastern California Shear Zone in the Ridgecrest-Trona region of California. The site is located in the north-west corner of San Bernardino County, approximately 200 kilometers north-east of Los Angeles, CA and about 234 kilometers south-

west of Las Vegas, NV (See Figure 3). Four mountain ranges are found in the region: the Cosos in the north, the Sierra Nevada Range in the west, the Argus Range in the east, and the El Paso Mountains in the south. In addition, five fault systems can be found in this region: the Owens Valley fault zone, Panamint Valley fault zone, Garlock fault zone, Blackwater fault zone, and San Andreas fault zone. Researchers are interested in this area because of the complicated interaction occurring between the faults, especially the San Andreas and Garlock, both faults which can produce large earthquakes. This area has limited vegetation and a small human presence, making it easy to observe surface changes. Ridgecrest is the most populous city in the area, with 27,616. Also, in the vicinity is the United States Navy's China Lake research facility, where most of the damage occurred. Researchers had limited access to investigate, so not much data exists from that area.

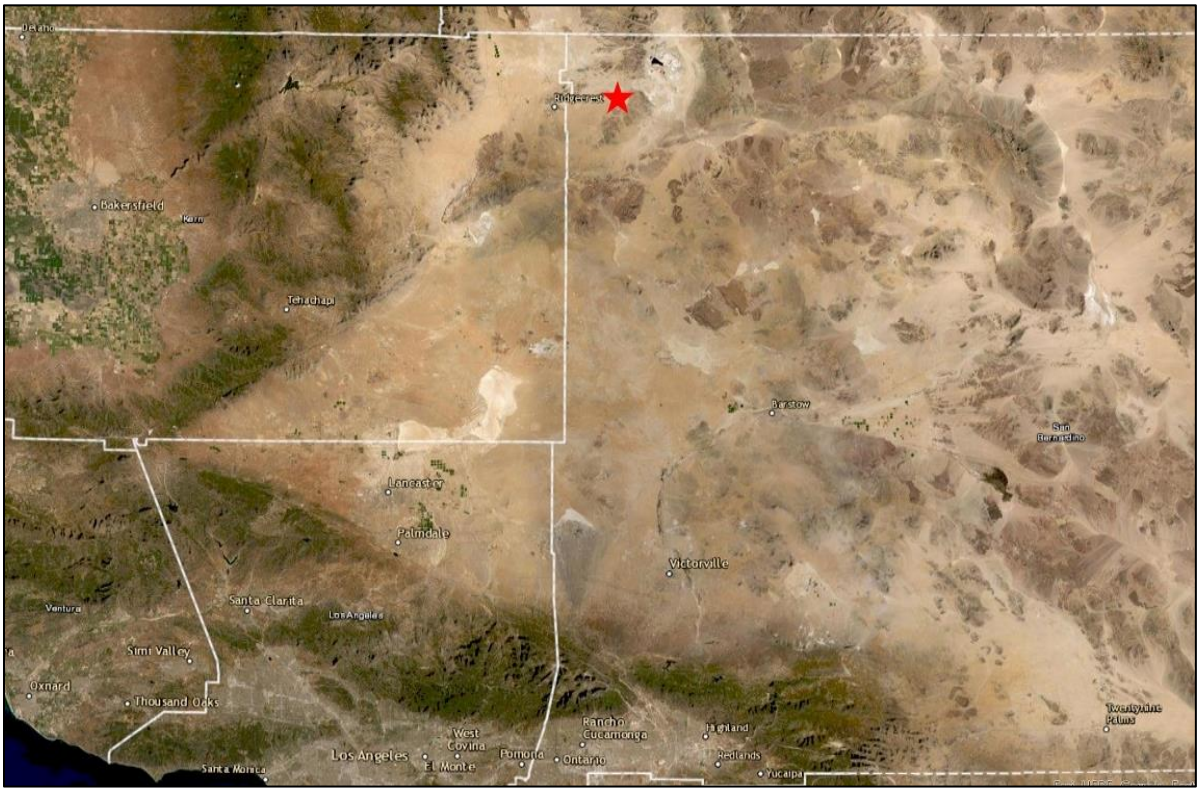

Figure 3 Location of the study site in north-west San Bernardino County.

The following chapter is a summary of research relevant to this thesis, starting with background information on the site and location. This includes an exploration of field data and remote sensed data collected from the Ridgecrest 2019 earthquake swarm. A detailed description of what data has been collected and analyzed is necessary to show how this project fits into the literature. Following is a look at the use of remote sensing and image classification of linear features. This is looked at to see what other potential methods are available for surface rupture detection. A short and broad look at supervised image classification comes next. Finally, the usage of aerial studies related to the detection of geologic features is presented. The rest of this thesis will be the following: methods used in this project, the results of the project, and the analyst of the results.

Chapter 2 Related Work

This report, like all research, benefits from a look at the related body of work that has been done in the past. To start, a look at the research that has been done related to the surface ruptures and surface damage that occurred at Ridgecrest and other seismic events. After this, linear feature detection is investigated. Following that will be a general look at supervised classification methods with more in-depth coverage of support vector machine classification. Finally, the last section of the chapter covers papers that used methods for the detection of linear geologic features.

2.1. Background

The 2019 Ridgecrest earthquake swarm created a rare opportunity for researchers to study surface ruptures with high-resolution equipment. Image data that was produced was extensive, including Aerial LIDAR from airplanes, High-resolution multi-spectral imagery from UAV's, and various forms of satellite imagery, both public and commercial. Each of these capture methods produced imagery that contain various optical properties of the study area. This makes it possible to classify the imagery through a GIS with different methodology.

Prior research into detecting damage from earthquakes through remote sensing means has been concentrated on satellite imagery and airplane mounted cameras. These images have been used to study the destruction of buildings and infrastructure following several major earthquakes such as the 1999 Chichi, Taiwan Earthquake, the 2003 Bam, Iran Earthquake, and the 2010 Haiti Earthquake (Dong and Shan 2013 and Fielding 2005). A common methodology that has been used to detect such damage has been change detection, which is a technique that involves a comparison of a before and after image. Early change detection algorithms would go through a pixel-by-pixel comparison, while modern algorithms usually perform an object-oriented

comparison. This technique is helpful for detecting significant changes such as when a building collapses, or a road becomes offset, but it is poor at discerning small changes such as surface ruptures. In addition, it is not helpful for situations in which there is not a before image or the before image is too much older than the after image. Based on this fact, new techniques that can rely on a single image are needed to detect surface ruptures and other seismic damage.

2.2. Linear Feature Detection

Remote sensing imagery has existed since the 1950s since the first satellites were sent into orbit by Russia and the United States. Following that time, the resolution of the imagery and the types of imagery collected advanced, leading to the ability to automatically detect objects in the 1970s. One of the early uses for the synthesis of remote sensing and automatic detection methods was the detection of roads and highways, objects that are sufficiently large enough to be detectable in the imagery of the time (Quackenbush 2004). Since the early days, the spatial resolution has continued to advance, allowing for smaller objects to be observed with greater accuracy.

In the utility industry, it has become commonplace to see linear object detection used. For example, in the electrical industry, remote sensing has been used to map out the locations of electrical towers and corridors in the early days. As new image capture methods have evolved, the applications have changed for the industry, with uses in the mid-2010s aimed at monitoring full grid status and fire safety along electrical corridors (Matikainen et. al. 2016). Methods used include airborne laser scanning synthetic aperture radar (SAR) images, optical satellite and aerial images, thermal images, airborne laser scanner (ALS) data, land-based mobile mapping data, and unmanned aerial vehicle (UAV) data capture (Matikainen et. al. 2016 and Guo et. al. 2016). All

these various tools have been brought together to create complete 3-D views of the electrical grid.

Another field that has benefited from linear object detection has been civil engineering. Within civil engineering, there has been an increase in studies related to crack detection in concrete (Mohan and Poobal 2018). These techniques are of particular interest to this thesis since the goal of this thesis is to detect cracks in a different scenario. Cracks, in our situation, are surface ruptures that should have similarities to those found in concrete, such as being linear and darker colored than the surrounding material.

Methods from industry are applicable to detect other linear features like surface ruptures but with one caveat. First, the algorithms used for detecting and monitoring these features have set rules which cannot be applied to ruptures. Pipelines, electric corridors, and roads have rules that are common, such as a line ends in a node or a water pipeline should connect to other lines. Surface ruptures also have rules that are as well established for where they occur. Many factors affect where surface ruptures arise, such as the geometry of local faults, soil and rock properties, and the strength of the earthquake that created it. Therefore, rules-based algorithms are not as useful for the detection of not just surface ruptures but other geologic lineaments as well.

2.3. Supervised Image Classification

Supervised classification methods are methods that involve a user creating training data with samples of the classifications that are of interest in remote sensed imagery. Supervised classification methods having a higher initial set up than unsupervised and can be more time-consuming, but it allows for some ground truthing to be incorporated into the classification process. Traditionally classification was done by pixel-based methods, but object-based methods

have gained popularity (Lei Ma et. al. 2016). This method groups pixels together using segmentation and classifies those segments based on what object the system predicts it to be.

Different object-based methods exist that are applicable to different scenarios, such as classifying different environments like urban, forest, or agricultural areas (Tehrany, Pradhan, and Jebuv 2013 and Duro, Franklin, and Dube 2012). Assorted methods are also best suited for work with rasters captured by various imaging systems like multi-spectral data or hyperspectral images. Amongst the many supervised classification techniques, Random Forest, K-Nearest Neighbor, and SVM are considered to have the highest level of accuracies and are the most used because of it (Thanh Noi and Kappas 2017). Amongst these three classification methods, the overall accuracy and results of their classification was similar if they had sufficiently large training sample size, around 0.25% of the research area. When below this value, SVM has been found to be the least affected by the size of the training data. SVM was selected for this reason, since the rupture lines are narrow areas of pixels in the rasters that are smaller than 0.25% of the area. Because the SVM classification is a core component of this thesis it is discussed in the following subsection.

2.4. Aerial Geologic Studies

Remote sensing has been a boon to the earth sciences since the first satellite images were captured, changing the way research is done. Since the early days of geologic field studies, research was done in person. Mapping of geologic features would be done this way; faults and folds could be found as what was seen in the field was drawn on the map. This changed with the development of one of the earliest forms of air travel, hot air balloons. A field mapper could go up and see the geology from a bird's eye view. As more advanced forms of air travel developed

and better cameras, more of the earth could be studied this way. The airplane, the rocket, and satellite, and now the UAV have all added to the available imagery of the earth's geology.

Studies of earthquake faults have used various remote sensing imagery to tease out the structure of faults. This has included standard methods such as LIDAR and SAR, but also less common field research tools such as UAVs that can detect changes in gravity anomalies or magnetic field changes in the subsurface. These specialized systems tend to be costly, so researchers use other cheaper methods such as InSAR. InSAR imagery is used to detect deformation that occurs following major seismic events. InSAR is one of the tools that has been used to create an image of the structure of the faults at depth. Surface ruptures occur along with earthquake faults, so understanding what is happening at depth helps researchers develop a complete image of what occurs at the surface, and the opposite is true too. For the Ridgecrest Earthquake Swarm, InSAR was a significant tool that was used along with surface rupture studies to find the geometry of the faults as well as the slip that occurred on them (Ross et. al. 2019)

Surface exposures of other linear geologic features have been detected as well, such as fault scarps. Research was performed in Slovenia to detect hard to observe fault scarps that were located in a forested area. To do this, researchers used a vegetation removal algorithm to remove trees in order to get a clear look at the topography. From there, they were able to visually inspect the topographic imagery and find fault scarps (Cunningham et. al. 2006). DEMs and DSMs have been a common tool for locating faults, such as when DEMS and satellite imagery were used to locate earthquake faults in the Black Forest, Germany (Meixner et. al. 2017). In another study, researchers used a LIDAR data collection to detect fault scarps in Northern California (Sare, Hilley, and DeLong 2019). This study used DEMs they generated in combination with template

matching algorithms to potentially detect segments of fault in the northern San Andreas Fault system. All of these examples show the importance of remote sensed imagery for detecting fault structures. A further consideration shows that combining it with various detection techniques creates powerful tools for finding fault exposures and other lineaments in hard-to-reach areas such as these.

UAV's have been used to collect imagery in several different areas of research in both the social sciences and the physical sciences. One area that is seeing increased usage as of 2020 is geologic studies. A significant component of geology is field research which is often done in demote, hard-to-reach areas. To study some of these sites' airplanes would be flown over to collect images of the site. Since then, though, UAVs have started to gain usage because of several advantages they have. UAVs are cheaper to fly than aircraft and can be used to image the same area over a small timespan. They are also able to reach areas that are hard to get to or hazardous to travel through, such as in a volcanic area or a landslide area. Another reason is that they can collect a high-resolution image normal to the surface and cover a larger area than a person on foot. The last reason is that cameras on some UAVs can be changed out, with each camera being able to collect imagery in different wavelengths, which can then be used to study various features.

Chapter 3 Methods

This study is composed of three general steps for the methods used: Data Integration, Image Classification, and Spatial Data Analysis. The first step, Data Preparation, looks at what data is used and what changes need to be made prior to classification. In the second step, (3.2) Image Classification, the imagery will be classified by SVM, a supervised technique that is readily available in ESRI's ArcPro 2.1. The last step, Spatial Data Analysis, (3.3) will involve an explanation of error matrices for the classification results and how it is used for the analysis. An overview of the steps can be seen in figure 4 below.

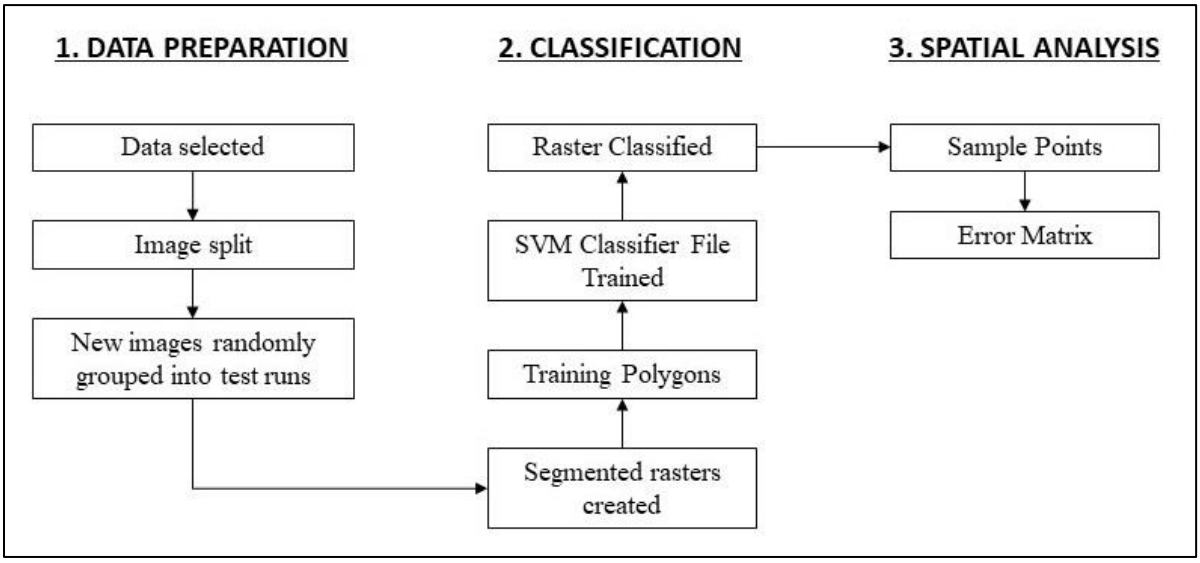

Figure 4 Flowchart of the steps involved in the methods used.

3.1. Data Preparation

This section covers: (3.1.1) the selection of the datasets for classification, (3.1.2) processing of the data to make it into a usable format, and (3.1.3) preparing it for creating training data for the object classification.

3.1.1. Data Selection

This thesis used two different files (see Table 1 below). The first data set is the UAV imagery that was downloaded from Geo-Gateway.org for a study site that covers an area of approximately 0.275 km^2 (Figure 5 below). This imagery contains a segment of surface rupture from the 7.1 Mw that is observable with the naked eye in the image, as well as several smaller strands that are harder to locate. Additional imagery was collected at this site on six other days, but due to time and data storage constraints, they were not used for this project. The second dataset is a line feature file of the surface ruptures produced by the United States Geologic Survey. In this data set, the data is generalized and considered preliminary.

Table 1 Data Metadata

Data	Name	File Type	Source	Scale	Precision	Accuracy	File Size
Surface Rupture Lines	Surface_Rupture Ridgecrest _Prov_Rel_1	.kml/.shp	USGS	Unknown	Unknown	< 10 m	32 MB
Drone Imagery	SVRL2019 0711C_ dsm_2cm	.laz/.las	https://archive. Geo-gateway. org:3000/ main.html	Multiscale	.5 m to 1.72 m	2 cm	1.5 GB

Figure 5 High resolution imagery of the study site with confirmed surface ruptures marked. Raster from Donnelan et al and lines from DuRoss et al.

Several remote sensed datasets related to the study site were found to be readily available; these datasets were collected with various electromagnetic spectra and methods. It was deemed acceptable for this project to use only one type of remote sensed data to simplify the project. In this case, a UAV imagery file that covered approximately 500 meters of the surface rupture from the Mw 7.1 earthquake. The UAV imagery has a high spatial resolution, with resolution approximately at 2 cm and an average ground sample distance of 1.68 cm. This dataset was taken on July 11th, seven days after the earthquake swarm began and five days after the Mw 7.1 mainshock occurred. The UAV imagery data is available in two different formats, a raw point cloud and a derivative digital surface model (DSM). Both file types have the same accuracy and spatial resolution, but the DSM files were selected for the classification in this project. The DSM file is preferred because it is a derivative of the point cloud that does not need further processing prior to classification. In addition, the DSM is a smaller file, which is a benefit when data storage is limited.

The UAV DSM imagery is composed of pixels that contain latitude and longitude data along with the three-color bands that contain the optical properties for the image. In addition, the surface elevation is also available in each pixel, which, along with the latitude and longitude data, is based on the coordinates collected at GPS stations. Donnellan et al. collected the imagery with a Parrot Anafi model UAV. The Anafi comes equipped with a 21-megapixel camera that took the imagery in a forward-facing direction, 20 degrees up from the nadir. The height of the flights was held at 45 m above ground level. Flights for the Mw 7.1 surface rupture segment were performed in the early afternoon for each of the flight days except one which was conducted in the morning. Like other common UAV's the Anafi has a limited flight time, up to approximately 25 minutes, that can cover only a small area.

Donnelan et al. (2020) used Pix4Dmapper software to create the orthomosaic and digital surface model raster from the imagery that the UAV collected (Figure 6 below). Pix4Dmapper created a quality report that contains information that is important to review when working with any data. The UAV collected 2432 images in total but only 2049 were used to create the DSM. The imagery was georeferenced using 11 ground control points with a RMS error of 0.016 m. That is a small RMS error meaning relative to the ground control points the imagery is accurately georeferenced. Figures showing the flight pattern can also be found in the quality report. These show how often the same location was visited. More in-depth accuracy measures can be found in the quality report.

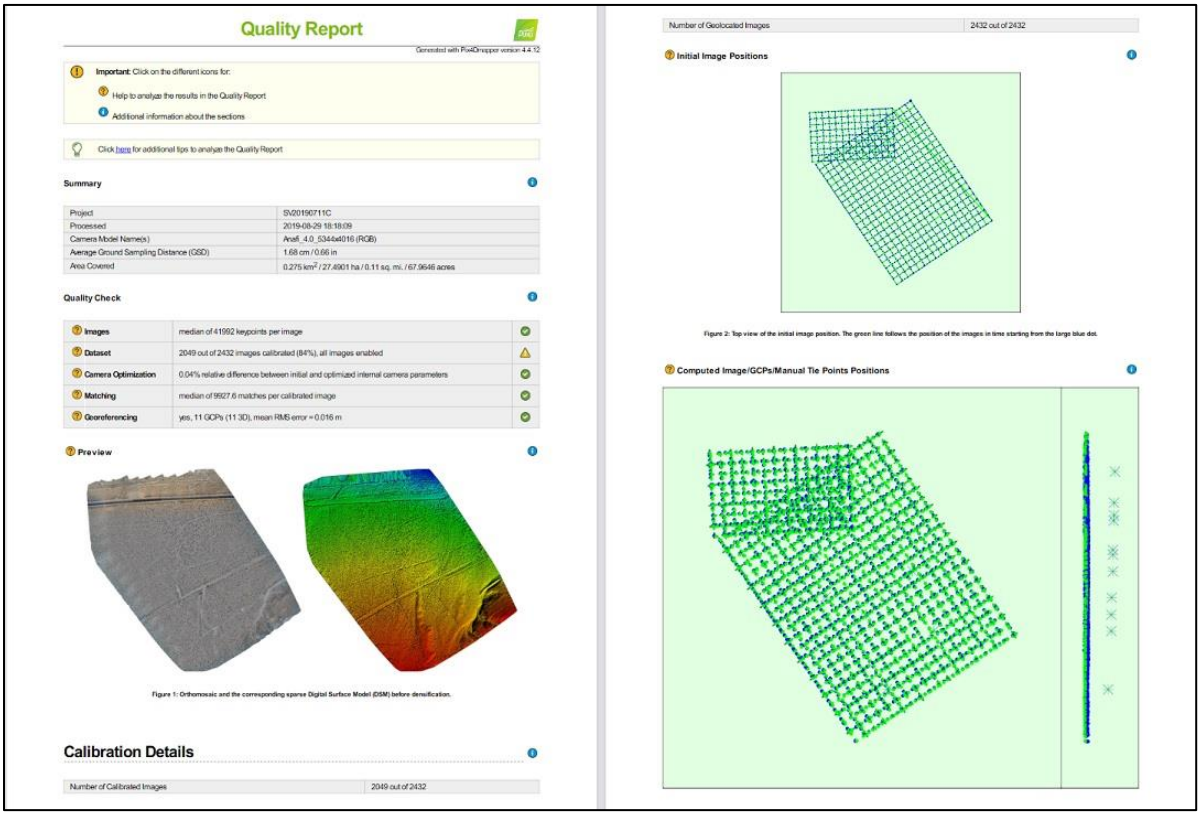

Figure 6 Sample of pages from quality report generated by Pix4Dmapper

The line file was originally a kml file the USGS released with the outline of the preliminary locations of the ruptures. Even though the line work is considered preliminary, it still has a high level of accuracy and has been validated in the field by the USGS. The file was imported into ArcGIS to use in the project as a a form of validation for the results of the classification. It was also visually compared to the raster imagery and found to match up closely.

3.1.2. Raster Format

High-resolution imagery, such as what was used in this project, is usually large, often reaching sizes greater than one gigabyte. The files were compressed to compensate for that and make the files easier to transfer or download. In the case of the UAV imagery that was used in this project, it was compressed with the laz compression format. The laz format is a standard compression format used to compress las files. The las file format is a raster format for LIDAR and high-resolution imagery. Las files contain 3-dimensional point cloud information, with each point containing x, y, and z data as well as the optical information at that point. The data was uncompressed in ArcGIS Pro with the Convert Las tool. All parameters in the tool were left as is. This tool converted the laz file to a las file. ArcGIS Pro displays LAS files as dots, so to make this usable, this format was then further processed with the LAS Dataset To Raster tool. Most of the parameters were left as is except for the sampling value, which was defined as .02 m and the file format selected was TIFF. TIFF is a common file format for rasters that ArcGIS Pro can export natively.

3.1.3. Data Preparation

The raster covered a small section of the overall surface rupture system in the area, 0.5 km of the 50 km of surface ruptures produced by the Mw 7.1 earthquake. This limited coverage of the site made it necessary to use a K-folds cross-validation method to ensure a statistically

significant number of tests were done. K-fold cross-validation is explained below in Section 3.3. The DSM file was split up into 30 meters by 30 meters grid using the Raster Split tool to generate the files that were used for the cross-validation. This yielded 274 separate raster files. 30-meters by 30-meters was chosen because it kept the number of the split rasters within a range that was not too many that it would be time-consuming to work with but also not too few that a statistical significance could not be reached.

3.2. Classification

A four-step process was used to perform the classification. First step was the segmentation of the data. This is a technique that the GIS performs to create a new raster where the pixels from the original raster are grouped together based on similar characteristics. The second step was the creation of training data for each of the training groups in the Training Sample Manager in ArcGIS Pro. When selecting training data, polygons were created that overlay the pixels in the imagery that represent the three categories of classification, "rupture," "no rupture," and "vegetation." In initial tests, additional categories were attempted for the classification schema, but these seemed to muddle the output and made each classification run several hours longer. Visual inspections of the results showed a decreased performance of the classification. The third step is to use the Train Support Vector Machine Classifier tool. This tool creates an Esri classifier definition file (ecd), which is a type of file that contains the attributes of the training results such as the hyperplane coordinates. The recommended max sample per class setting of 1000 was found to be acceptable for this tool. To confirm this, various values for this setting were tried on a small test area before the project was attempted. It was found that an increase in number of sampling beyond 1000 did not produce a noticeable change in classification but significantly increased the processing time for the tool. The final step was to

use the ecd file in the Classify Raster tool with the test samples. In this project, the tool uses the training data to find whether a pixel belongs to the "rupture," "no rupture," or "vegetation" category. This generated the final classified rasters that were then analyzed.

3.3. Spatial Analysis

The goal of this part of the thesis is to check the accuracy of the classification outputs created by the methods used. To check for the accuracy quantitatively, error matrices were created for each test run. Error matrices are table outputs that are created when one compares a dataset with expected values to the classified dataset. Prior to an error matrix being created in ArcGIS, random sample points are made using the Create Accuracy Assessment Points tool. This generates points that contain the classified value at that location and requires the user to input the expected value. These values are used in the calculation of the error matrix.

The error matrix table contains information on the results of the accuracy assessment points as well as the producer accuracy, user accuracy, total accuracy, and kappa coefficient. Producer accuracy is how likely is what is found in the original raster will be found in the classified image. This is tied to errors of omission (Equation 1 below), which are those values that were omitted by the classifier, so in this case, any surface rupture pixels that are missing. User accuracy, on the other hand, is how likely what is found in the map matches with what is observable in the field. This is tied to the errors of commission (Equation 2 below), which are those values that were improperly classified as the classification of interest; in this case, it is those pixels that are classified as "surface rupture" when they should have been "not surface rupture" or "vegetation". Total accuracy is the overall accuracy of the classification, but it is an average across all the classes. Because it is an average, one does not see if any individual classes are more or less accurate than the other classes. This is why user accuracy and producer accuracy

are critical to check for each class. The last statistical measure looked at is the kappa coefficient. Kappa is a measure of likeliness that results are due to the classification software or random chance. Kappa is a value from -1 to 1, with a value closer to 0, meaning that the results are random and a value closer to 1, indicating the results are due to the classification. The coefficient is calculated by comparing the actual results to expected results (Equation 3 below).

Equation 1: Producer Accuracy = 100% - Omission Error

Equation 2: User Accuracy = 100% - Commission Error

Equation 3: Kappa Coeffiecent = (Actual Results - Predicted Results) / (1 – Predicted Results)

For this project, we are primarily interested in the correct classification of surface ruptures from the imagery, but the overall accuracy of the classification of vegetation and non-rupture surfaces is also investigated. Both the errors of commission and errors of omission were looked at to check the accuracy to quantify how well the overall methodology worked. Five error matrices were created, once for each of the 5-Fold cross validation runs. The Producer Accuracy and User Accuracy from the five runs were then averaged out to find the resulting accuracy of the method. Kappa coefficient is also looked at to check whether the results are due to the classification algorithm or just a random result.

Usually when testing a classification method, such as SVM, it is necessary to run several different tests to remove any potential biases that would occur in a single test run. This is not possible with a small data set so the K-folds cross-validation is used instead. K-folds cross-validation is a validation technique that is useful when working with a small data set, since it less likely to be affected by biases (James 2017). When using K-folds the researcher randomly splits

the data into equal sized pools. The training data creation and classification is ran a number of times equal to the number of pools. Each of these test runs will use a pool as a test group while the rest will be used for training data. After a pool has been used a new pool is selected and the last pool joins the training data. When all the data has been used once, the results are averaged out creating the final assessment. As stated before, the averaged out results should limit the effect of biases found in any one testing pool.

Typical K-fold cross validation is done with somewhere from 5 to 10 test groups. In the case of this thesis a 5-fold cross-validation method was used to cross-validate the data. This means that every test was composed of a randomly selected mix of images, with 80% being used to generate the ecd training files and 20% being used to test the training files and create the classified rasters for validation. To do this, the split images were assigned a number, and those numbers were randomly selected to make each test pool. Every image only participated in one test pool.

Chapter 4 Analysis

Chapter 4 is separated into two sections. The first of the sections is the results for two of the five test runs, which will be presented and analyzed (Section 4.1). The second section is the evaluation of the overall results for the entire data set. (Section 4.2).

4.1. Test Results

The first four test runs were composed of 69 of the 30-meter by 30-meter rasters that were split off from the original raster by the Split Raster tool. The fifth test run was composed of 68 raster portions. Features found throughout the original raster were observed to be distributed between all five test runs. All the figures for this section can be found in Appendix A except for the figures for Test Run 1 (4.1.1.) and Test Run 4 (4.1.2). Error matrices for Test Runs 2, 3, and 5 can be found in Appendix B. In each test run, the typical components of the original raster were found throughout the group on split rasters. These components include the desert surface, paths, dry streambeds, paved roads, rocks, and shrubs. In addition, some discoloration can be found in the sections of the imagery towards the edges of the image. This discoloration shows up as a blue tint on the eastern and western sections and orange in the northern section. There is also a minor blue tint in the southern part of the map that is not as prevalent as the discoloration in the other edges. It is relevant to be aware of the discoloration around the edges since that changes the properties of the raster cells at those locations. When creating the training polygons, those sections were avoided to prevent issues with placing the boundaries between the classes in the training file.

Results from two of the five test runs are covered in this section (4.1.1 – 4.1.2.). These two test runs were selected to represent the range of results where one consists of a poor result and one that represents a good result. For each test run, the classified raster was visually

inspected prior to the creation of the error matrix. Observations from those inspections are discussed first. Second, a small discussion of the results of the error matrix will follow.

4.1.1. Poor Test Results - Test Run 1

Portions of the original raster that were used in the first test can be seen below in Figure 7. For this test run, one of the crucial parts of the raster is the small segment of the main surface rupture that can be found in the center of the study site, which is circled in figures 7 and 8, and a larger version is in Figure 9. The rupture can be seen in the lower-left square as a line in the desert surface with some dark soil around it in figure 9. In figure 9, there is a section of pink that traces that same area, showing that the classification method did capture the main surface rupture in that area. A large area appears to be captured, which includes disturbed soils around the surface rupture as well as the rupture itself. Similarly, this can be seen in the square north-west of those, providing additional evidence that the main surface rupture is detectable by the SVM classification method. On the other hand, it does not appear to capture the thinner segments that are present. It also seems to misclassify the paths and stream beds as "rupture." Much of the shrubbery and non-surface rupture areas appear to be adequately classified, with obvious exceptions being the aforementioned paths and streams, as well as the edges of the study area, the rock field in the south-east corner, and the road to the north.

Figure 7 Randomized 30x30m rasters used for Test Run 1. Circled area shown in closer detail in Figure 9.

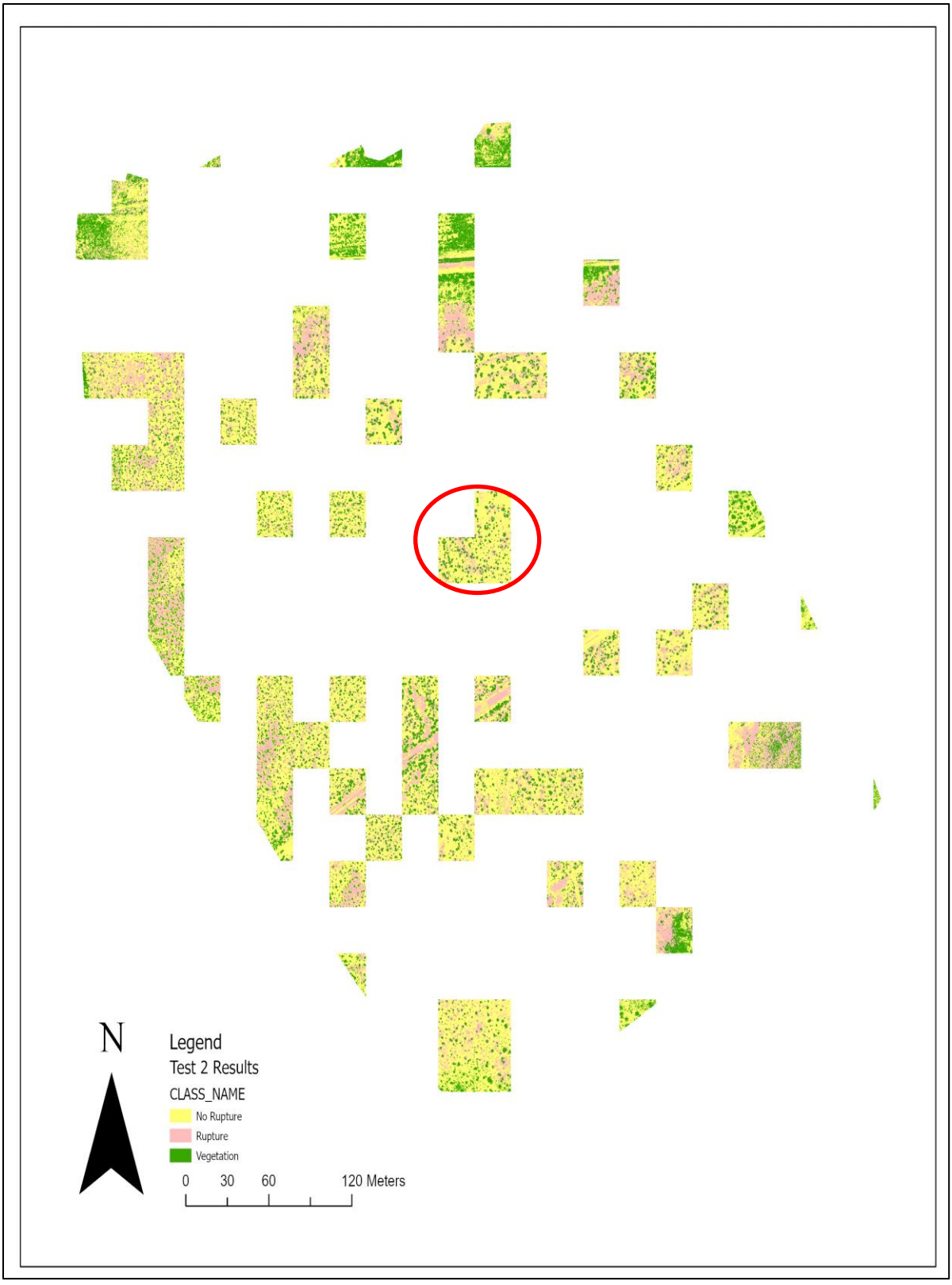

Figure 8 Classified Results of Test Run 1, classified with SVM classifier. Circled area shown in closer detail in Figure 9.

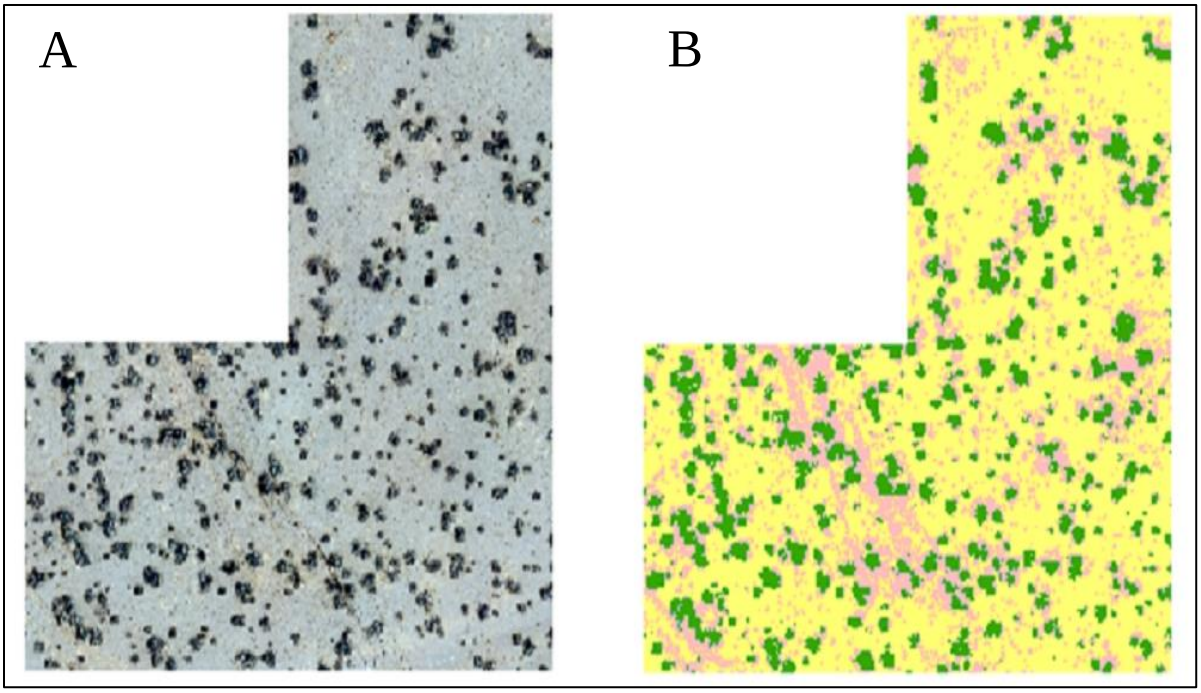

Figure 9 Comparison of the main surface rupture observed in the original raster (A) and the classified raster (B) for Test Run 1.

The confusion matrix shows that the classification of Test Run 1 was a mixed result (Table 2). The "no rupture" classification had a user accuracy of 96.7%, which means that only a small amount of the other classes was classified as "no rupture." When looking at the producer accuracy for the same class, one sees that many of the "rupture" cells were included, this in combination with the small number of "vegetation" misclassification caused a drop in the accuracy to 68.3%. "rupture" cells counted for only a small number of the total cells in the classification, so any errors have a substantial effect on the accuracy. This is why the user accuracy is at only 6.8% for the "rupture" class, with 105 "no rupture" and 17 "vegetation" cells being classified as "rupture" versus only nine cells being correctly classified as "rupture." The surface ruptures are narrow lines that limit the available cells to classify. Producer accuracy is also affected by this fact, so even though it resulted in a 90.0%, it needs to be carefully

considered when analyzing the results. The final class, "vegetation," had good results, with a producer accuracy of 76.9% and user accuracy of 83.8%. "Vegetation" is distinct from the desert surface, with the dark coloration of the vegetation being easy to distinguish from the light colors of the desert. This helped in the consistent classification, though the edges of the vegetation would blend with the desert surface immediately next to it, which is likely why the results were average. Overall, the total accuracy was 70.6%, which was dragged down by the "rupture" user accuracy results, as well as the producer accuracy results for "no rupture." Finally, the Kappa coefficient can be looked at, which was .454. Kappa coefficients do not have exact breakdowns for what each coefficient value means, though the fact that it is closer to zero means that the results were only slightly better than random chance. All of these results point to Test Run 1 not being successful at capturing the surface rupture in a way that is meaningful, especially for a user of the map.

Table 2. Confusion Matrix (or Error Matrix) for Test Run 1

Class Value	No Rupture	Rupture	Vegetation	Total	User Accuracy	Kappa
No Rupture	261	1	8	270	96.7%	
Rupture	105	9	17	131	6.9%	
Vegetation	16	0	83	99	83.8%	
Total	382	10	108	500		
Producer Accuracy	68.3%	90.0%	76.9%		70.6%	
Kappa						0.454

4.1.2. Good Test Results - Test Run 4

Test Run 4 is composed of the portions of the original raster found below in Figure 10. This test run, like all the test runs, has segments of the surface ruptures in various portions of the map. A segment of the primary surface rupture is circled below in both the original raster in

figure 10 and in the classified raster seen in Figure 11. A larger version of the surface rupture is found in figure 12. The fault is a dark line that cuts diagonally from north-west to south-east across both image portions. In the matching classified image, the surface rupture is clearly captured. There are small pockets of the “rupture” class also seen in the image along the paths, but they do not stand out as much as the classified surface rupture. The SVM classification was even able to capture the separate strands of the rupture in the upper left square. Test Run 4 appears to have been the best classification of all the tests, with not just the main surface rupture classified but parts of the smaller ruptures as well. Like the other test runs, there was distortion along the edges of the raster from the color tint, which caused widespread misclassification in those areas. In addition, there was misclassification in the rock field area in the south-east.

Figure 10 Randomized 30x30m rasters used for Test Run 4. Circled area shown in closer detail in Figure 12.

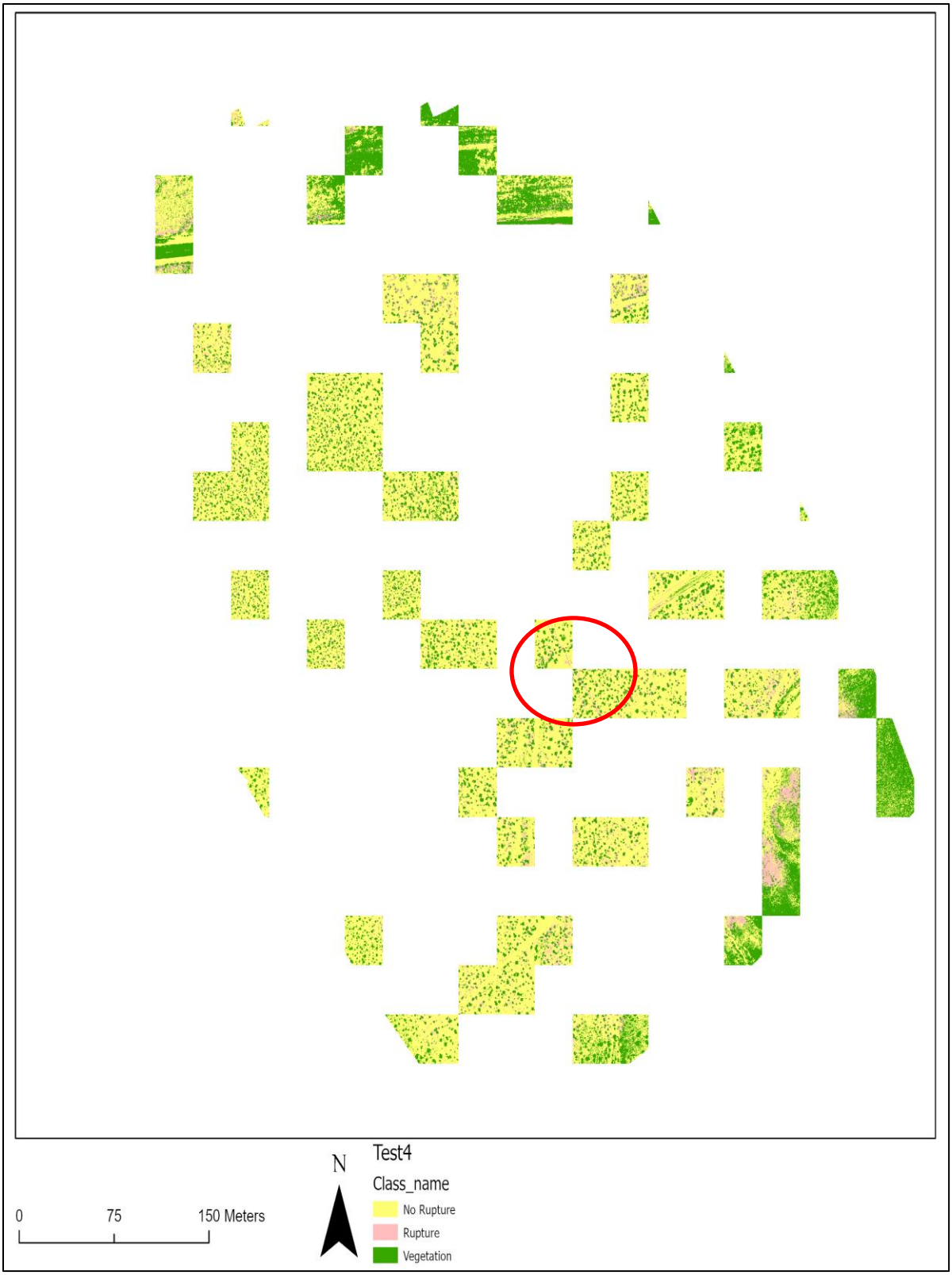

Figure 11 Classified Results of Test Run 4, classified with SVM classifier. Circled area shown in closer detail in Figure 12.

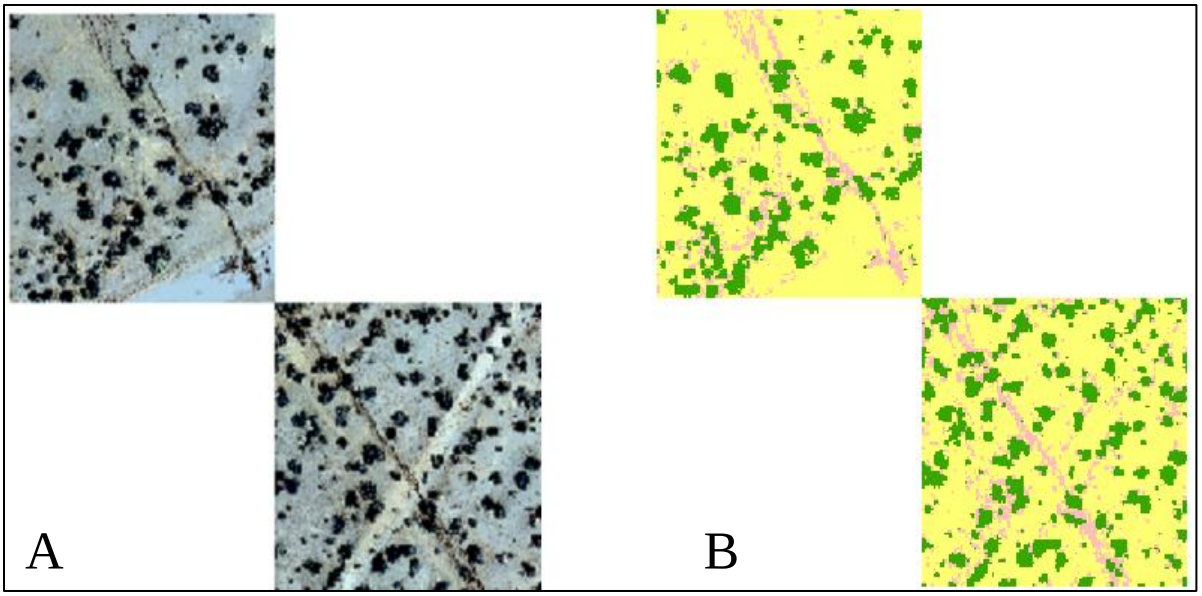

Figure 12 Comparison of the main surface rupture observed in the original raster (A) and the classified raster (B) for Test Run 4.

For the classification of Test Run 4, the error matrix had primarily good results (Table 3). The "no rupture" class had a user accuracy of 98.9% and a producer accuracy of 89.6%, making it the most accurately classified class in any of the tests. A small number of the "rupture" class was thrown into both, which is expected since surface rupture is formed in the desert surface. The training data used may have had a small amount of "rupture" pixels mixed in with "no rupture," and vice versa as well. "Rupture" class results were okay at 18.8% for the user accuracy, better than any of the other test runs. The producer accuracy was lower than the other classes, though, at 69.2%. As previously stated, the results for the "Rupture" class need to be carefully considered since the surface rupture is a small portion of the study site. “Vegetation” was also highly accurate, with user accuracy of 82.5% and a producer accuracy of 83.3%. All these results led to a good total accuracy of 87.8%. This is higher than any of the other test runs, which in combination with the visual inspection of the classified raster, shows that this was a successful test run. The final part of the confusion matrix to look at is the Kappa coefficient. Test

Run 4 has the highest kappa coefficient of all test runs at 0.7. The score is close to 1, which means that the classification results were not likely caused by random chance. Unlike Test Run 1, all of the results for Test Run 4 show that with good training data, large surface ruptures can be captured with the SVM classification method.

Table 3. Confusion Matrix (or Error Matrix) for Test Run 4

Class Value	No Rupture	Rupture	Vegetation	Total	User Accuracy	Kappa
No Rupture	344	3	1	348	98.9%	
Rupture	23	9	16	48	18.8%	
Vegetation	17	1	85	103	82.5%	
Total	384	13	102	499		
Producer Accuracy	89.6%	69.2%	83.3%		87.8%	
Kappa						0.7

4.2. Overall Results

This part is similar to the previous sections, but it is a look at the overall results across all five test runs. This includes a look at a map with the combined results, as well as averages of the results of the five confusion matrix results, except for the kappa coefficient.

The results from all five test runs were brought together, as shown in Figure 13 below, to get a better understanding of how effective the classification method is. Underneath is Figure 14, which is Figure 13 with the addition of the linework from the USGS for comparison purposes. There are several features that stand out when first looking over the complete picture. One observation is that the road and paths in the original raster are traced out accurately in the image. The paths stand out because of the lack of "vegetation" found in them, while the "no rupture" class usually has "vegetation" dispersed throughout. This shows that the methodology used was able to differentiate "vegetation" and "no rupture." Another observation is the misclassification

that occurred along the edges of the raster. This highlights the effect of the discoloration in the original raster image. That discoloration has caused the cells in those areas to have the wrong optical properties, so the classification placed them in a different class based on how the training data was binned. In the south-east corner, there is also a large section of “vegetation," which is a group of misclassified cells that should have been "no rupture." That area is a rock field that has optical properties that are different from any other part of the raster. This could be corrected in future runs of the methodology by creating an additional class, though this will increase processing time. It is also important to point out the large areas of the raster that are classified as "rupture" that should be placed into another class. Those are from Test Runs 1 and 2 and appear to have occurred because of the training data that was used. This is based on the fact that all of the settings and methods stayed the same between the tests, but a more significant amount of training data was used for the last three test runs.

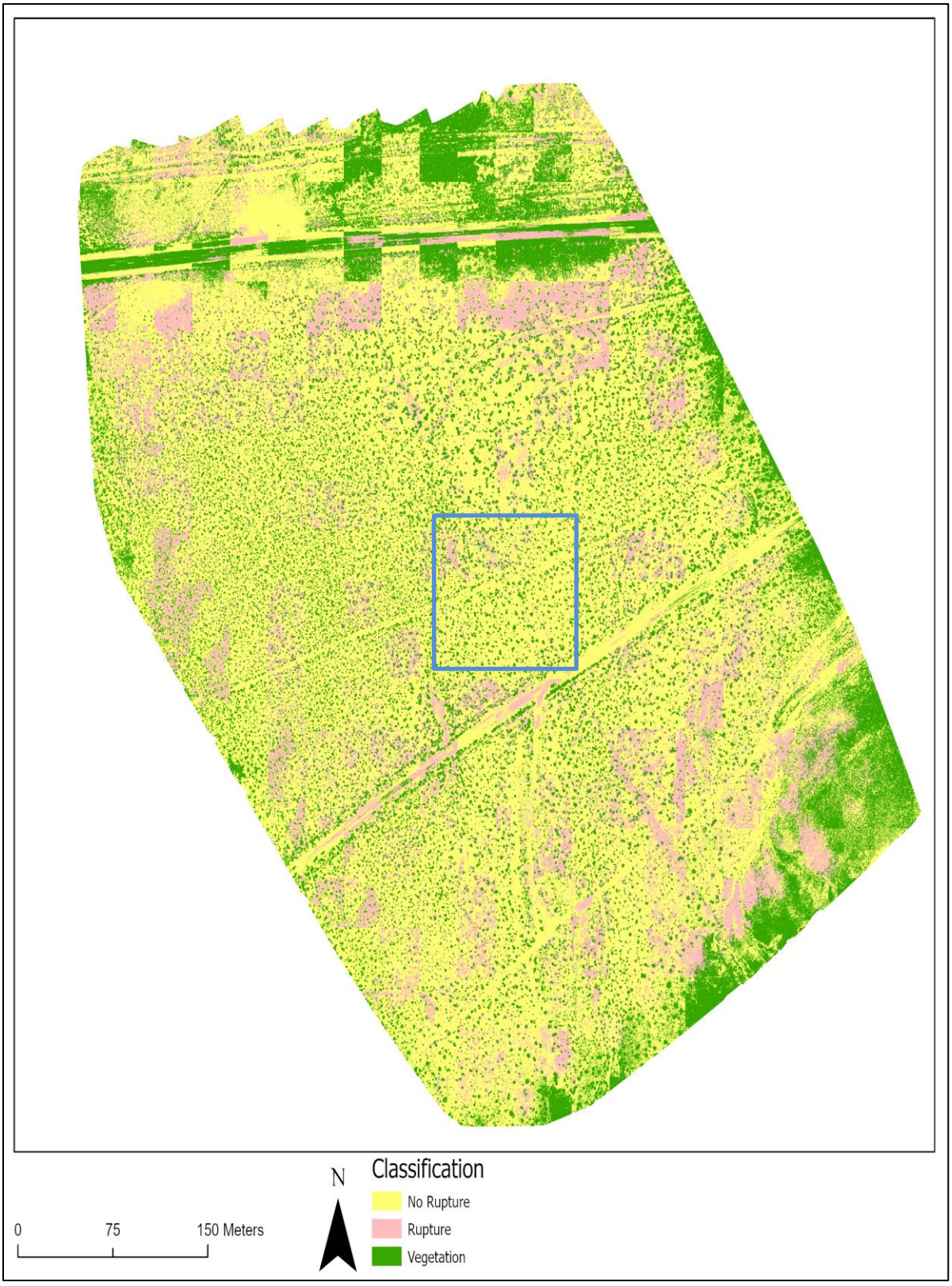

Figure 13 Classified Results of all 5 Test Runs. Close up of area in square in Figure 15 and 16 below.

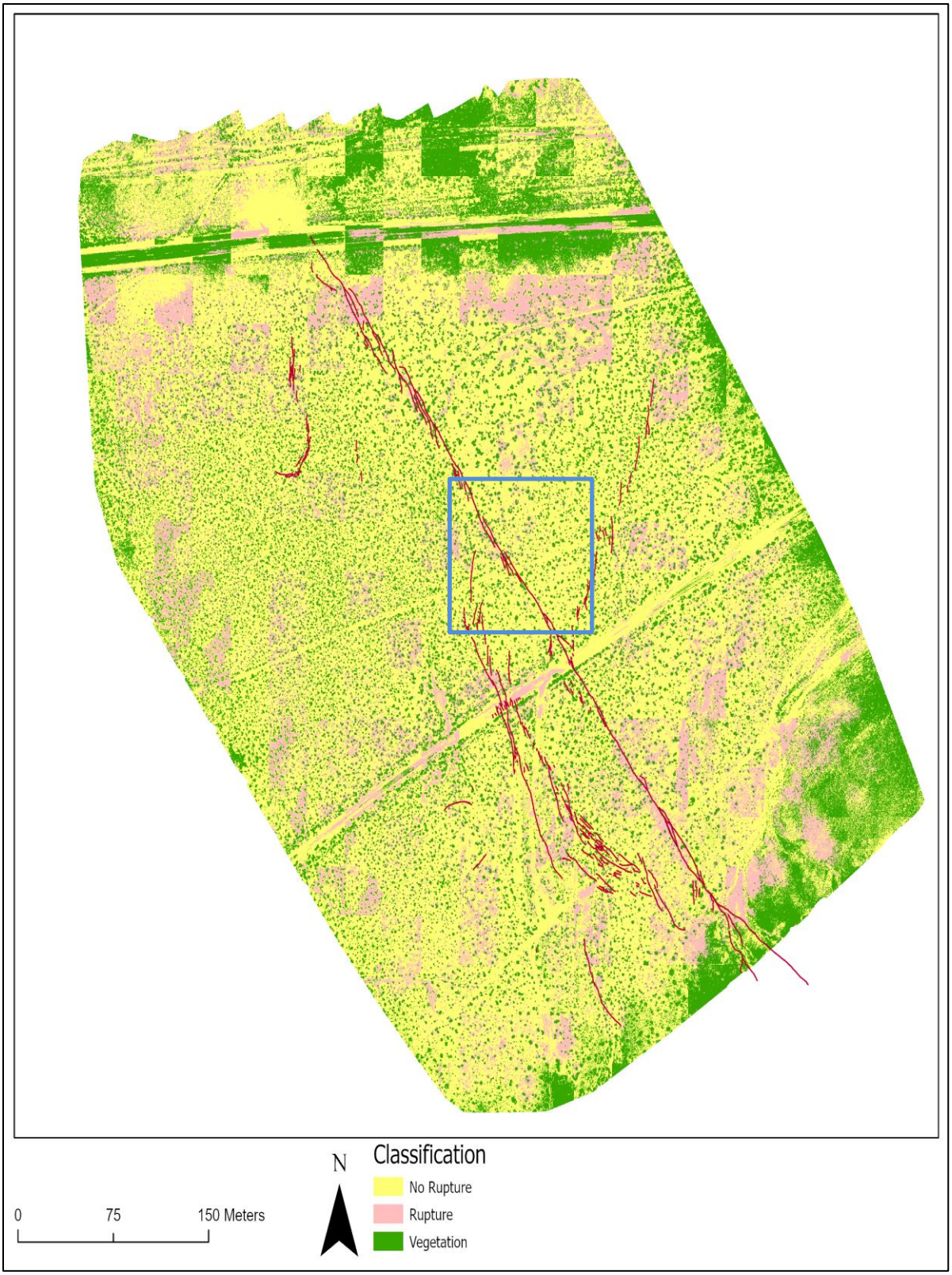

Figure 14 Classified Results of all 5 Test Runs with surface rupture lines. Close up of area in square in Figure 15 and 16.

Finally, the success of the method at classifying the surface ruptures needs to be examined. Figures 15 and 16, found below, show a sample of the classification of the rupture and the rupture lines laid over it. Looking at the image, one can see that the main rupture is well classified and easily distinguishable from any other features in the image. It is even possible to observe individual branches of the rupture. When the image is magnified further, some smaller surface ruptures are also observable though not to the same degree. Groups of "rupture" pixels form linear patterns along those lines, but there are breaks along the linear patterns, showing that it is not capturing the entire rupture. Overall, all the methodology appears to work though the results would be better if the first two test runs were replaced with test runs like the latter three.

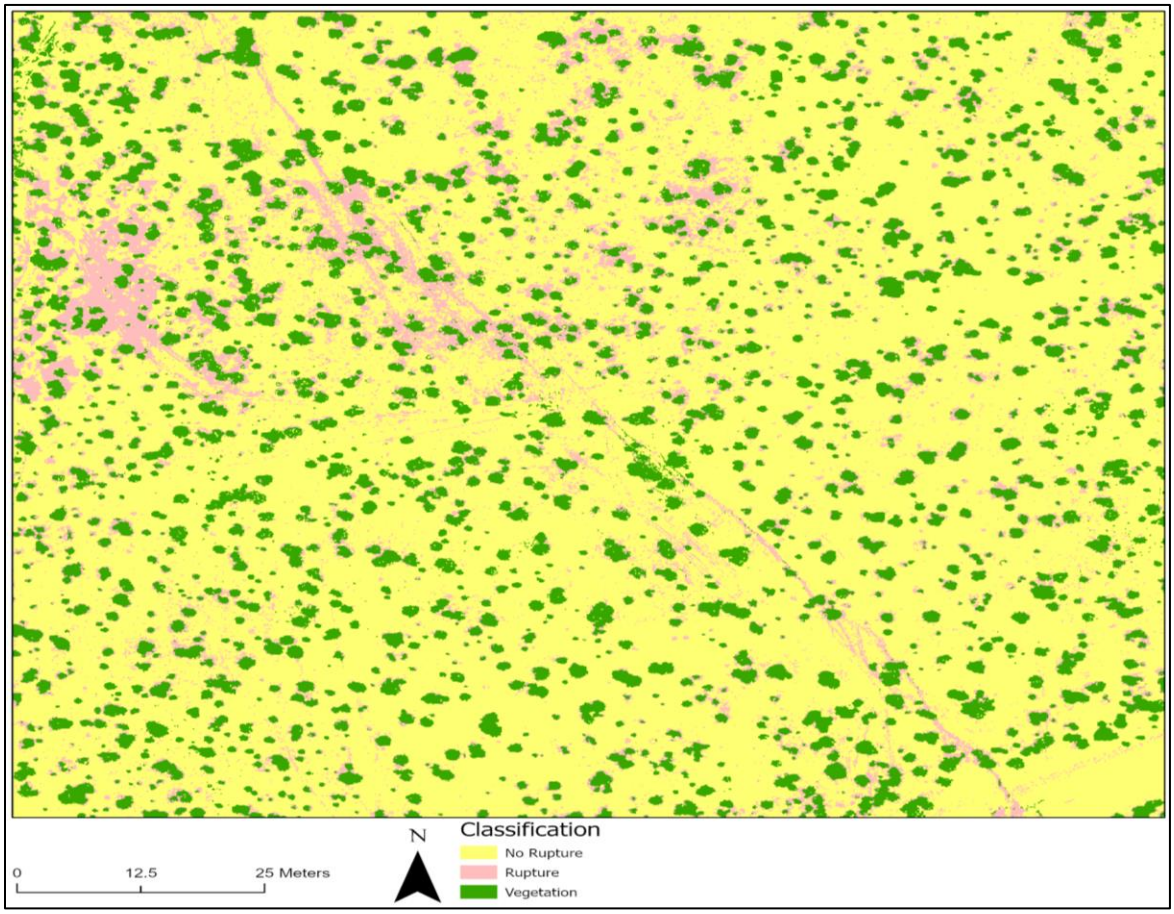

Figure 15 Close up of surface rupture segment.

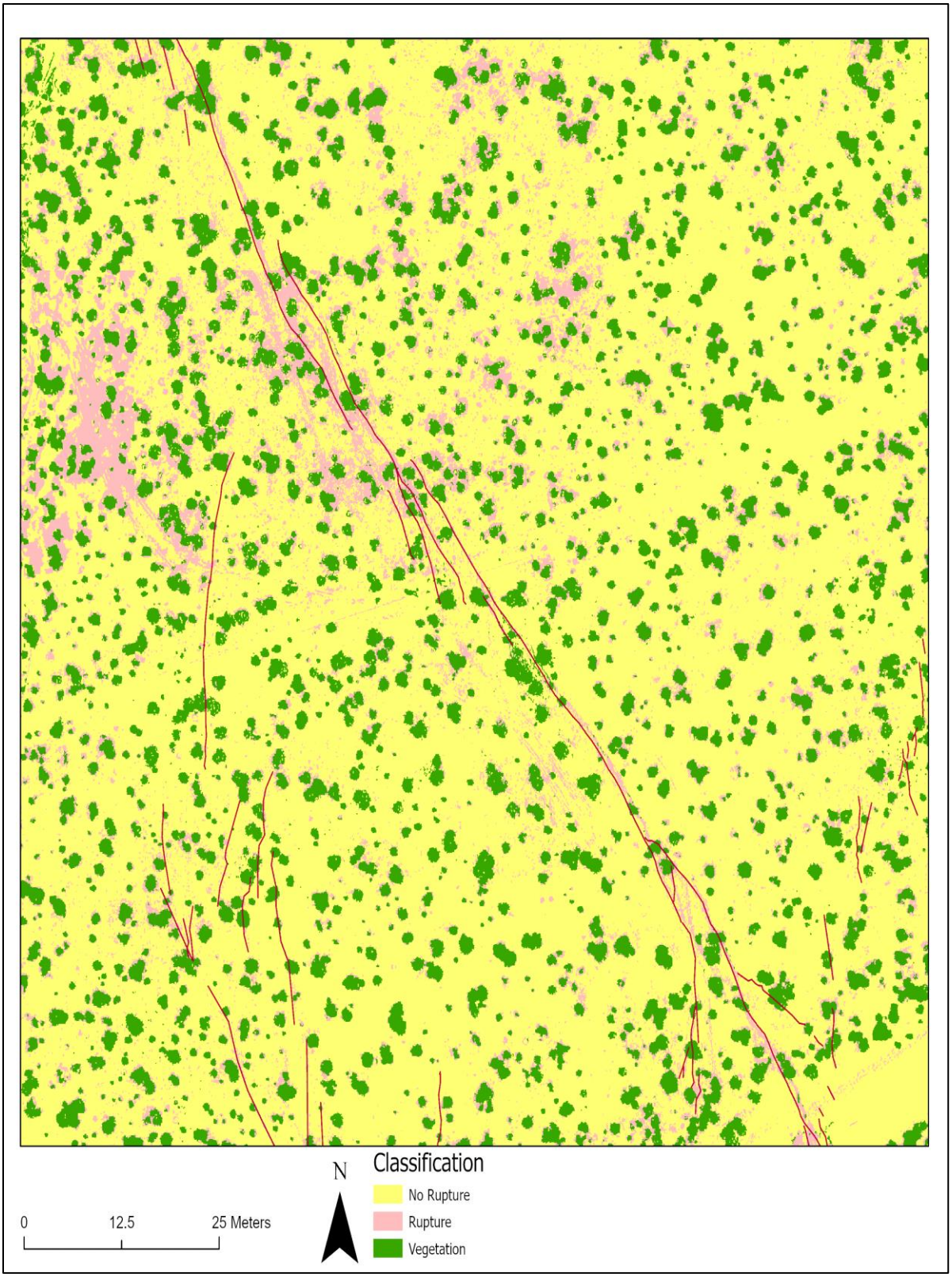

Figure 16 Close up of surface rupture segment with ground truthed surface rupture lines from USGS.

Creating an average of the results of all the confusion matrices reveals the overall success of the classification though some issues are found (Table 4). The "No rupture" class had a user accuracy of 97.0% and 77.0%, which shows that the classification method was highly effective at detecting and classifying the class. This was the largest class across the entire raster, as evidenced by the number of sampling points correctly classified in the confusion matrix. The results are trustworthy based on this fact. The second-largest class was “vegetation," which also had good results, with a user accuracy of 78.0% and a producer accuracy of 75.6%. When comparing the results of the classifications and the original raster, it can be seen how well the SVM classification is able to differentiate between the classes. That is expected since the optical properties are highly distinct between the two. The next class to look at is the “rupture” class, the smallest class by a large degree. Only 47 sample points out of 2496 were classified correctly as "rupture," so the results may be skewed because of this small sample size. User accuracy for this class is exceptionally low at 10.0%, which would typically point to the method failing at detecting the "rupture" cells, though this may not be true. It is likely that the results are influenced by the poor results from Test 1 and Test 2, as well as the low number of sample points in the confusion matrix. Producer accuracy is close in value to the other classes at 77.1%. Like the individual test runs, this result needs to be carefully considered based on the low sampling. The averaged total accuracy for all the tests is at 76.7%, which is a good result, but it does not reflect the poor outcome of the "rupture" user accuracy. Results for the kappa coefficient were not included since it cannot be averaged from the results of the five matrices.

Table 4. Confusion Matrix (or Error Matrix) for Combined Test Runs

Class Value	Not Rupture	Rupture	Vegetation	Total	User Accuracy
Not Rupture	1463	11	33	1508	97.0%
Rupture	324	47	98	469	10.0%
Vegetation	112	2	405	519	78.0%
Total	1899	61	536	2496	
Producer Acc.	77.0%	77.1%	75.6%		76.7%

Chapter 5 Discussion

The results of this project showed that the proposed methodology is only partially applicable, as is, to this research site. In order to assess this, the classification results from each test were compared to a dataset with the known locations of the surface ruptures. SVM was able to capture the primary section of fault rupture but failed to capture the smaller strands of the ruptures. In addition, it misclassified some of the paths and streams, or at least the edges, and the areas around bushes as rupture. It is not clear why this is, but the areas around bushes likely have similar optical properties to the soil disturbed by the surface rupture. This may be because the shrubs are casting a shadow, or they may keep the soil moister, or it could be the decay of material from the bushes. These are all possibilities but finding the cause is beyond the scope of this project. Paths and streams were most likely misclassified because they share some similarities with the ruptures. The ruptures probably share some level of linearity with them, as well as similar coloration, likely caused by the fact that in these cases, the soil has been disturbed, which reveals lower soils.

It is important to note that the training data used seems to have a substantial effect on the results of this project. The first two test runs did not seem to get as accurate of a classification of the main surface rupture as the last three test runs. While everything was kept consistent between the five tests, the only difference was the number of training sample polygons used for training the classifier. If Test Runs 1 and 2 had the same volume of training data, the resultant combined user accuracy would have been higher. From this, one can infer that an overabundance of training samples does not hurt classification in this case.

If this method had worked, it would have been a boon to response teams following earthquakes and possibly other hazards. Despite it appearing to not work fully as intended,

similar methods, such as those used by Zhang et al, have worked before. This shows that the method has potential that should be further researched. Anything that can accelerate the detection of hazardous areas that rescue and repair crews can target following a natural disaster is essential to help save people.

5.1. Future Work

5.1.1 Additional Data Sets

As mentioned previously, when the software was classifying the imagery, parts of the study area were misclassified. This is because the optical properties the classification tool is detecting are similar between the rupture and regions around the paths and bushes. One solution for dealing with this is the inclusion of other datasets that cover different parts of the electromagnetic spectrum. The best type of imagery dataset that may help with this is hyperspectral imagery. While the multi-spectral imagery used in this study is composed of three bands, hyperspectral imagery is usually composed of over one hundred bands. Each band is composed of a small segment of the light spectrum. With hundreds of small bands, the software would be able to bin a smaller range of values for the rupture classification and likely decrease the number of misclassified pixels. A possible way to analyze the additional raster imagery is to use Empirical mode decomposition (Adu-Gyamfi et. al. 2011). This method takes the imagery of various resolutions and breaks them apart into smaller band components that represent unique differences between the imagery. Those smaller components can be recombined or filtered to bring out linear features.

5.1.2 Methods Outside of ArcGIS

ArcGIS is limited in the number of tools that are natively available for classification. There are other methods that may be better suited for extracting the fault ruptures from imagery,

such as those covered in Mohan and Poobal's (2018) review on crack detection in concrete. These methods should be applicable since the properties of the concrete cracks should be like those of fault ruptures. Both are linear features, usually not straight, and considerably darker than the surrounding surface.

Some, if not all, of the methods that were used can be done in the Python programing language with readily available libraries. ArcGIS already includes a python compiler and its own python library. Python can be used to integrate ArcGIS functions with some of these various libraries, such as those used for machine learning, like TensorFlow or Pytorch. Bringing python into this would open up a large number of new methods for performing this research.

5.1.3 Computational Performance Increase

Data storage and time became issues when performing this project. This entire project was performed on a virtual desktop that has limited storage and can only be accessed for 5 hours at a time. These factors constrained the processed that could be performed to only those that fit into that time frame and the allotted storage. If these limits were not in place, additional testing on the imagery for the Mw 6.4 or performing the methods on the imagery from the six other days could have been performed. This would have added to this project, creating more statistically significant results to the project, but the space needed was far more than was available. So, in the future, it would help to perform this on a desktop computer which can be left on for processes to be completed and data issues are easier to manage. There were 14 total UAV images from the two sites across the seven days that were available. A model could be created to run the steps that were performed on the image used for this thesis without interruption. The only human input needed would be the initial creation of the training data.

5.1.4 Additional Scenarios

Methods used in this project need to be tested in other locales besides a desert area like Ridgecrest, CA. Imagery collected from other types of terrain will have different spectral properties than those in the imagery used in this project. One type of terrain it would be beneficial to test in is urban and suburban areas. These areas have more buildings, more underground utilities, and higher populations. Being able to quickly locate areas that have been damaged will help save lives. A forested area would also be an area to consider testing in. The tree cover makes it hard to observe the ground surface in this sort of environment, but it is possible to capture imagery of it with a LiDAR system. These terrains, and other settings, have their own qualities that can hinder the observation of the fault ruptures. Working out how to deal with these hindrances ahead of time is a criterion for applying this methodology to the real world.

Testing it in a real-world scenario, or at least a simulation of one, would also be insightful. One of the usages for this method is to use it for directing safety crews to the location of the damage but to make sure it assists them with their duties; testing needs to be performed. The simulation can include different situations, such as locating damaged roads, utilities, or buildings and any individuals hurt by those hazards. It could be integrated into a dashboard that can find the rupture and be used to estimate damage costs, track first responders, keep track of hospital loads, or any other piece of information that policymakers, first responders, and other members of government need.

References

Adu-Gyamfi, Y. O., N. O. Okine, Gonzalo Garateguy, Rafael Carrillo, and Gonzalo R. Arce. "Multiresolution Information Mining for Pavement Crack Image Analysis." *Journal of Computing in Civil Engineering* 26, no. 6 (2012): 741–749.

Anniballe, Roberta, Fabrizio Noto, Tanya Scalia, Christian Bignami, Salvatore Stramondo, Marco Chini, and Nazzareno Pierdicca. "Earthquake Damage Mapping: An Overall Assessment of Ground Surveys and VHR Image Change Detection after L'Aquila 2009 Earthquake." *Remote Sensing of Environment* 210 (2018): 166–178.

Ci, Tianyu, Zhen Liu, Ying Wang, Qigen Lin, and Di Wu. "An Automated Technique for Damage Mapping after Earthquakes by Detecting Changes between High-Resolution Images" (2018).

CRED. Natural Disasters 2019. Brussels: CRED; 2020.

Cunningham, Dickson, Stephen Grebby, Kevin Tansey, Andrej Gosar, and Vanja Kastelic. "Application of Airborne LiDAR to Mapping Seismogenic Faults in Forested Mountainous Terrain, Southeastern Alps, Slovenia." *Geophysical Research Letters* 33, no. 20 (2006).

Dong, Laigen, and Jie Shan. "A Comprehensive Review of Earthquake-Induced Building Damage Detection with Remote Sensing Techniques." *ISPRS Journal of Photogrammetry and Remote Sensing* 84 (2013): 85–99.

Donnellan, Andrea, Gregory Lyzenga, Adnan Ansar, Christine Goulet, Jun Wang, and Marlon Pierce. "Targeted High-Resolution Structure from Motion Observations over the Mw 6.4 and 7.1 Ruptures of the Ridgecrest Earthquake Sequence." *Seismological Research Letters* 91, no. 4 (2020): 2087–2095.

DuRoss, Christopher B., Gold R., Dawson, T., Scharer, K.., Kendrick, K., Akciz, S., Angster, S., Bachhuber, J., Bacon, S., Bennett, S., Blair, L., Brooks, B., Bullard, T., Burgess, W.P., Chupik, C., DeFrisco, M., Delano, J., Dolan, J., Frost, E., Graehl, N., Haddon, E., Hatem, A., Hernandez, J., Hitchcock, C., Hudnut, K., Jobe, J.T., Koehler, R., Kozaci, O., Ladinsky, T., Madugo, C., McPhillips, D., Milliner, C., Morelan, A., Olson, B., Patton, J., Philibosian, B., Pickering, A.J., Pierce, I., Ponti, D., Seitz, G., Spangler, E., Swanson, B., Thomas, T., Treiman, J., Valencia, F., Williams, A., and Zinke, R.. Surface Displacement Observations of the 2019 Ridgecrest, California Earthquake Sequence: U.S. Geological Survey data release. (2020).

Duro, Dennis C., Steven E. Franklin, and Monique G. Dubé. "Multi-Scale Object-Based Image Analysis and Feature Selection of Multi-Sensor Earth Observation Imagery Using Random Forests." *International Journal of Remote Sensing* 33, no. 14 (2012): 4502–4526.

Duro, Dennis C., Steven E. Franklin, and Monique G. Dubé. “A Comparison of Pixel-Based and Object-Based Image Analysis with Selected Machine Learning Algorithms for the Classification of Agricultural Landscapes Using SPOT-5 HRG Imagery.” *Remote Sensing of Environment* 118 (2012): 259–272.

Fielding, E. J. “Surface Ruptures and Building Damage of the 2003 Bam, Iran, Earthquake Mapped by Satellite Synthetic Aperture Radar Interferometric Correlation.” *Journal of Geophysical Research* 110, no. B3 (2005).

Guo, Bo, Qingquan Li, Xianfeng Huang, and Chisheng Wang. “An Improved Method for Power-Line Reconstruction from Point Cloud Data.” *Remote Sensing* 8, no. 1 (2016): 36.

Jain, Sanjay, and Ashok K Dubey. “Image Change Detection for Earthquake Damage Assessment.” *International Journal of Advanced Research in Computer Science* 2, no. 5 (2011): 85–89.

James, Gareth, Daniela Witten, Trevor Hastie, and Robert Tibshirani. Essay. In *An Introduction to Statistical Learning: with Applications in R*, 181–182. New York, New York: Springer, 2017.

Jin, Kwangmin, and Young-Seog Kim. “The Importance of Surface Ruptures and Fault Damage Zones in Earthquake Hazard Assessment: a Review and New Suggestions.” *Geological Society, London, Special Publications* (2019).

Lei Ma, Manchun Li, Xiaoxue Ma, Liang Cheng, Peijun Du, Yongxue Liu. “A review of supervised object-based land-cover image classification.” *ISPRS Journal of Photogrammetry and Remote Sensing* 130, (2017): 277-293.

Li, Zhengrong, Rodney Walker, Ross Hayward, and Luis Mejias. “Advances in Vegetation Management for Power Line Corridor Monitoring Using Aerial Remote Sensing Techniques.” *2010 1st International Conference on Applied Robotics for the Power Industry (CARPI 2010)* (2010).

Matikainen, Leena, Matti Lehtomäki, Eero Ahokas, Juha Hyyppä, Mika Karjalainen, Anttoni Jaakkola, Antero Kukko, and Tero Heinonen. “Remote Sensing Methods for Power Line Corridor Surveys.” *ISPRS Journal of Photogrammetry and Remote Sensing* 119 (2016): 10–31.

Meixner, J., J.C. Grimmer, A. Becker, E. Schill, and T. Kohl. “Comparison of Different Digital Elevation Models and Satellite Imagery for Lineament Analysis: Implications for Identification and Spatial Arrangement of Fault Zones in Crystalline Basement Rocks of the Southern Black Forest (Germany).” *Journal of Structural Geology* 108 (2018): 256–268.

Mohan, Arun, and Sumathi Poobal. “Crack Detection Using Image Processing: A Critical Review and Analysis.” *Alexandria Engineering Journal* 57, no. 2 (2018): 787–798.

Quackenbush, Lindi J. “A Review of Techniques for Extracting Linear Features from Imagery.” *Photogrammetric Engineering & Remote Sensing* 70, no. 12 (2004): 1383–1392.

Ross, Zachary E., Benjamín Idini, Zhe Jia, Oliver L. Stephenson, Minyan Zhong, Xin Wang, Zhongwen Zhan, et al. “Hierarchical Interlocked Orthogonal Faulting in the 2019 Ridgecrest Earthquake Sequence.” *Science* 366, no. 6463 (2019): 346–351.

Sare, Robert, George E. Hilley, and Stephen B. DeLong. “Regional-Scale Detection of Fault Scarps and Other Tectonic Landforms: Examples From Northern California.” *Journal of Geophysical Research: Solid Earth* 124, no. 1 (2019): 1016–1035.

Sofina, Natalia, and Manfred Ehlers. “Building Change Detection Using High Resolution Remotely Sensed Data and GIS.” *IEEE Journal of Selected Topics in Applied Earth Observations and Remote Sensing* 9, no. 8 (2016): 3430–3438.

Tehrany, Mahyat Shafapour, Biswajeet Pradhan, and Mustafa Neamah Jebuv. “A Comparative Assessment between Object and Pixel-Based Classification Approaches for Land Use/Land Cover Mapping Using SPOT 5 Imagery.” *Geocarto International* 29, no. 4 (2013): 351–369.

Thanh Noi, Phan, and Martin Kappas. “Comparison of Random Forest, k-Nearest Neighbor, and Support Vector Machine Classifiers for Land Cover Classification Using Sentinel-2 Imagery.” *Sensors* 18, no. 2 (2017): 18.

Zhang, Fan, Zhenqi Hu, Yaokun Fu, Kun Yang, Qunying Wu, and Zewei Feng. “A New Identification Method for Surface Cracks from UAV Images Based on Machine Learning in Coal Mining Areas.” *Remote Sensing* 12, no. 10 (2020): 1571.

Appendix A: Test Run 2 Raster, Classification, and Error Matrix

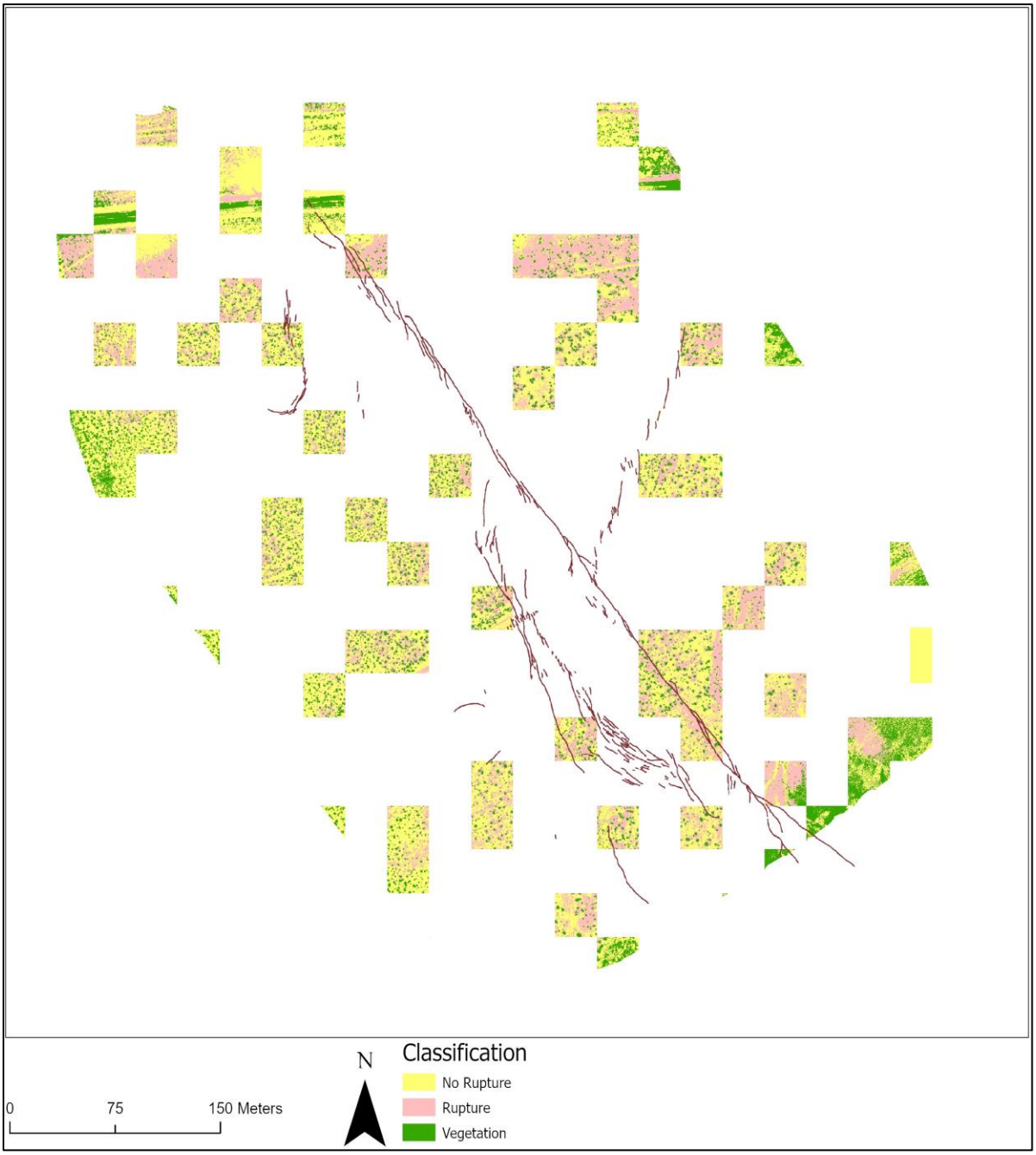

Class Value	No Rupture	Rupture	Vegetation	Total	User Accuracy	Kappa
No Rupture	227	3	8	238	95.4%	
Rupture	136	13	27	176	7.4%	
Vegetation	16	0	70	86	81.4%	
Total	380	16	104	500		
Producer Accuracy	59.7%	81.3%	67.3%		62%	
Kappa						0.358

Appendix B: Test Run 3 Raster, Classification, and Error Matrix

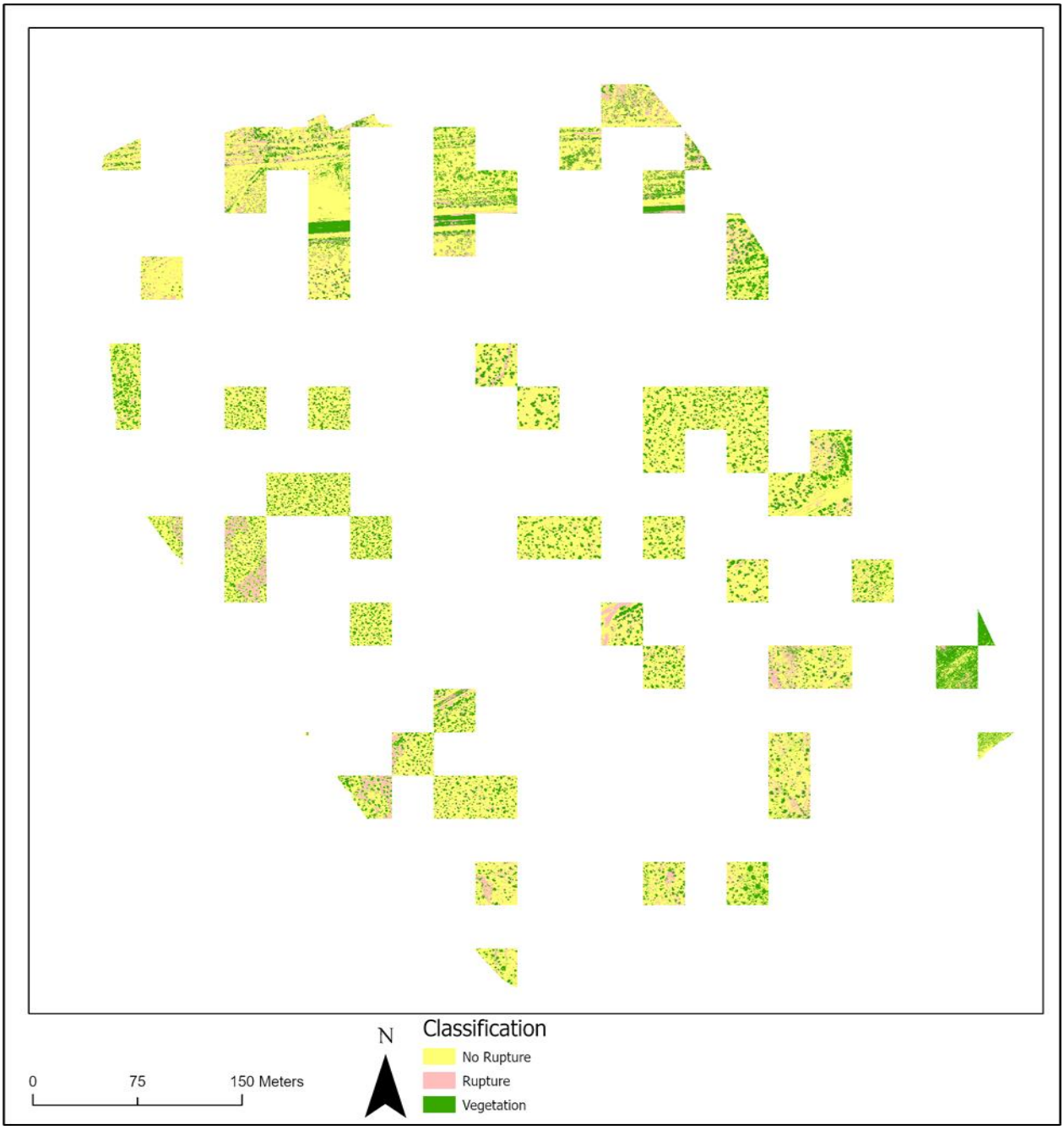

Class Value	No Rupture	Rupture	Vegetation	Total	User Accuracy	Kappa
No Rupture	322	1	10	333	96.7%	
Rupture	40	6	19	65	9.1%	
Vegetation	30	1	70	101	69.3%	
Total	392	8	99	499		
Producer Accuracy	82.4%	66.7%	70.7%		79.8%	
Kappa						0.531

Appendix C: Test Run 5 Raster, Classification, and Error Matrix

Class Value	No Rupture	Rupture	Vegetation	Total	User Accuracy	Kappa
No Rupture	309	4	6	319	96.6%	
Rupture	20	10	19	49	20.0%	
Vegetation	33	0	97	130	74.6%	
Total	362	14	122	500		
Producer Accuracy	85.1%	71.4%	78.9%		83.5%	
Kappa						0.645